Research Square

Preprints are preliminary reports that have not undergone peer review.
They should not be considered conclusive, used to inform clinical practice,
or referenced by the media as validated information.

Topographic Amplification at the Eastern Anatolia Observatory Site: A Comparative Analysis

Mehmet Ozyazicioglu

mehmetoz@atauni.edu.tr

Atatürk University

Cahit Yesilyaprak

Türkiye National Observatories, DAG

Case Report

Keywords: Topographic amplification, Seismic site effects, Horizontal-to-Vertical Spectral Ratio (HVSR), Standard Spectral Ratio (SSR), Nakamura method, Observatory site, Eastern Anatolia

Posted Date: October 30th, 2026

DOI: https://doi.org/10.21203/rs.3.rs-11119370/v1

License: This work is licensed under a Creative Commons Attribution 4.0 International License.
Read Full License

Additional Declarations: No competing interests reported.

Topographic Amplification at the Eastern Anatolia Observatory Site: A Comparative Analysis

Mehmet Ozyazicioglu[1,2,*] (0000-0002-4313-2973)
Cahit Yesilyaprak[1] (0000-0003-1894-7190)
[1] Türkiye National Observatories, DAG, 25050, Erzurum, Türkiye
[2] Department of Civil Engineering, Atatürk University, Erzurum, Türkiye
*Corresponding author, mehmetoz@atauni.edu.tr

Abstract

This study investigates topographic site amplification at the Eastern Anatolia Observatory (DAG) site. It uses data from the 16 September 2022 Çat earthquake of magnitude Mw 4.9. The event was recorded by internationally registered seismic stations, ETEKE and EKONA. ETEKE is at the mountain base, while EKONA is approximately 55 m below the summit. We apply two methods to estimate frequency‑dependent amplification. These are the Standard Spectral Ratio (SSR) and the Horizontal‑to‑Vertical Spectral Ratio (HVSR). The SSR compares spectra at the target site to a reference rock site and provides absolute amplification values. The HVSR method provides a single-station estimate of the fundamental resonant frequency. We also compare the results with two different seismic codes, which provide provisions for topographic amplification. Our results reveal a clear topographic resonance at 0.85 Hz. The SSR amplification factors at this frequency are 3.35 (E), 4.52 (N), with a geometric mean (GM) of 3.89. The HVSR analysis also identifies the same 0.85 Hz peak. While the two methods are not independent, the absence of the 0.85 Hz peak at ETEKE and consistency with response spectra support the topographic amplification. The pseudo−acceleration response spectra (PSA) ratio at T = 1.18 s is 1.80. This value exceeds the maximum topographic amplification factors in the seismic codes by 28%. While these results are derived from a single earthquake, the absence of the peak at the base station, the response-spectra consistency, and an independent ambient-noise H/V measurement supports the findings. However, the findings should be considered preliminary and require validation with future earthquake recordings. A moving-block bootstrap analysis yields uncertainty estimates that support the statistical significance of the results. The findings highlight the potential importance of site-specific, frequency-dependent topographic amplification for infrastructure at steep terrain. However, because the analysis is based on a single event at one azimuth, the comparison with the codes should be treated as preliminary, requiring validation with additional earthquake recordings.

Keywords: Topographic amplification, Seismic site effects, Horizontal-to-Vertical Spectral Ratio (HVSR), Standard Spectral Ratio (SSR), Nakamura method, Observatory site, Eastern Anatolia

1. Introduction

Topographic amplification is the increase in seismic ground motion at hills, ridges and mountain crests, where ground slope changes occur. This effect has been recognised as a critical factor in earthquake hazard assessment, and extensively studied. Seismic waves interact with irregular surface topography, and undergo diffraction/focusing and resonance (Aki and Richards, 2002). Theoretical studies by Boore (1972) were among the first to demonstrate that simple topographic features can amplify SH waves. As a result of these interactions, ground motion amplitudes may grow to exceed those on flat ground. This phenomenon has been documented in numerous earthquakes, including the 1985 Mexico City, 1989 Loma Prieta and 1994 Northridge events. Borcherdt and Gibbs (1976) demonstrated that local geological conditions can significantly amplify ground motions and influence the distribution of earthquake damage. Theoretical and numerical studies have since confirmed that local topography leads to complex amplification patterns (Sanchez-Sesma and Campillo, 1991; Faccioli, 1991; Bouchon et al., 1996; Assimaki et al. 2005; Sun and Li, 2012; Zhou, 2018).

The Eastern Anatolia Observatory (DAG) observatory is situated on G2 Peak (3151 m) of Palandöken Mountain Range. The telescope and its optical components are vulnerable to seismic shaking. This vulnerability and the high precision requirements of astronomical observations necessitates characterisation of site-specific seismic amplification. The DAG site currently hosts the 4‑m infrared telescope, along with various facilities and buildings around the telescope. Adjacent peaks G1, G3, and G4 remain undeveloped but are allocated for future projects that may include larger telescopes. Thus, the seismic characterisation of the DAG site is not only critical for the existing telescope but also provides a baseline for the expansion of the observatory's 2500 m^2 campus.

A probabilistic seismic hazard assessment for the DAG site was conducted by Ozyazıcıoğlu et al. (2024). However, that study did not account for local topographic amplification, which can significantly increase ground motions at the summit. The present study complements the PSHA work by empirically quantifying the site-specific amplification at Karakaya Peak using the 16 September 2022 Çat earthquake of Mw 4.9. This event was recorded by two weak motion (velocity) stations, one at the base (ETEKE, 2137 m) and the second (EKONA, 3096 m) close to the summit, provide a valuable opportunity to evaluate topographic amplification. First, since both stations were installed on firm rock (see section 2.2), the relative amplification involves mostly the topographic effects. Secondly, weak−motion recordings are widely used for site−response studies (Borcherdt, 1970; Steidl et al., 1996; Pitilakis, et al. 2013). For moderate earthquakes, they capture amplification effectively without the risk of instrument clipping. Clipping often occurs during large earthquakes and can compromise data quality. The Çat earthquake recordings are therefore well suited for this analysis.

To evaluate frequency-dependent amplification, we employ two well-established empirical methods, the Standard Spectral Ratio technique introduced by Borcherdt (1970) and the Horizontal-to-Vertical Spectral Ratio method by Nakamura (1989). The SSR provides the amplification relative to a reference rock site. The HVSR method assumes that the vertical component is relatively unaffected by site effects and identifies the fundamental resonance frequency (Bard, 1999; Yalcinkaya and Alptekin, 2005; Maufroy et al., 2015).

We compare our empirical results with the topographic amplification factors in the French seismic code PS92 (NF P06-013, 1995) and Eurocode 8 Part 5 (European Committee for Standardization, 2004b). Both codes give frequency independent factors. PS92 uses τ = 1.0 - 1.4 based on slope geometry. Eurocode 8 prescribes S_t = 1.0 – 1.4 according to topographic class.

The comparison reveals an important point. The pseudo−acceleration response spectra (PSA) ratio at 0.85 Hz is 1.80. This value exceeds the maximum code factors (τ = 1.4 for PS92; St = 1.4 for EC8). This suggests that the code factors are not adequate for broadband design at this site.

2. Site Description and Geological Setting

2.1 The DAG Observatory Site

Figure 1a shows the regional setting of the DAG site within the Eastern Anatolian fault system and the epicentre of the 16 September 2022 Mw = 4.9 Çat earthquake. Figure 1b illustrates the local topography around the observatory. Figure 1b is obtained from the SRTM 90 m digital elevation model (Jarvis et al., 2008), which provides 3-arcsecond (≈90 m) spatial resolution. Figure 2 shows a Google Earth profile of the site from the mountain base to G2 Peak. The profile reveals a steep lower section with a maximum slope of 49.1%. The upper section is gentler with an average slope of 19.1%. The two seismic stations ETEKE and EKONA are situated at the base and near the peak, respectively. The mountain range is aligned approximately in East-West direction; the azimuth of the ridge axis is 78°. But the local ridge axis at the DAG site is oriented NE-SW with azimuth approximately 58.5° from North; both angles are extracted from the SRTM DEM (Jarvis et al., 2008). This local bend in the ridge reflects the segmented geometry of the range. Hence this asymmetric topography is expected to produce frequency-dependent seismic amplification.

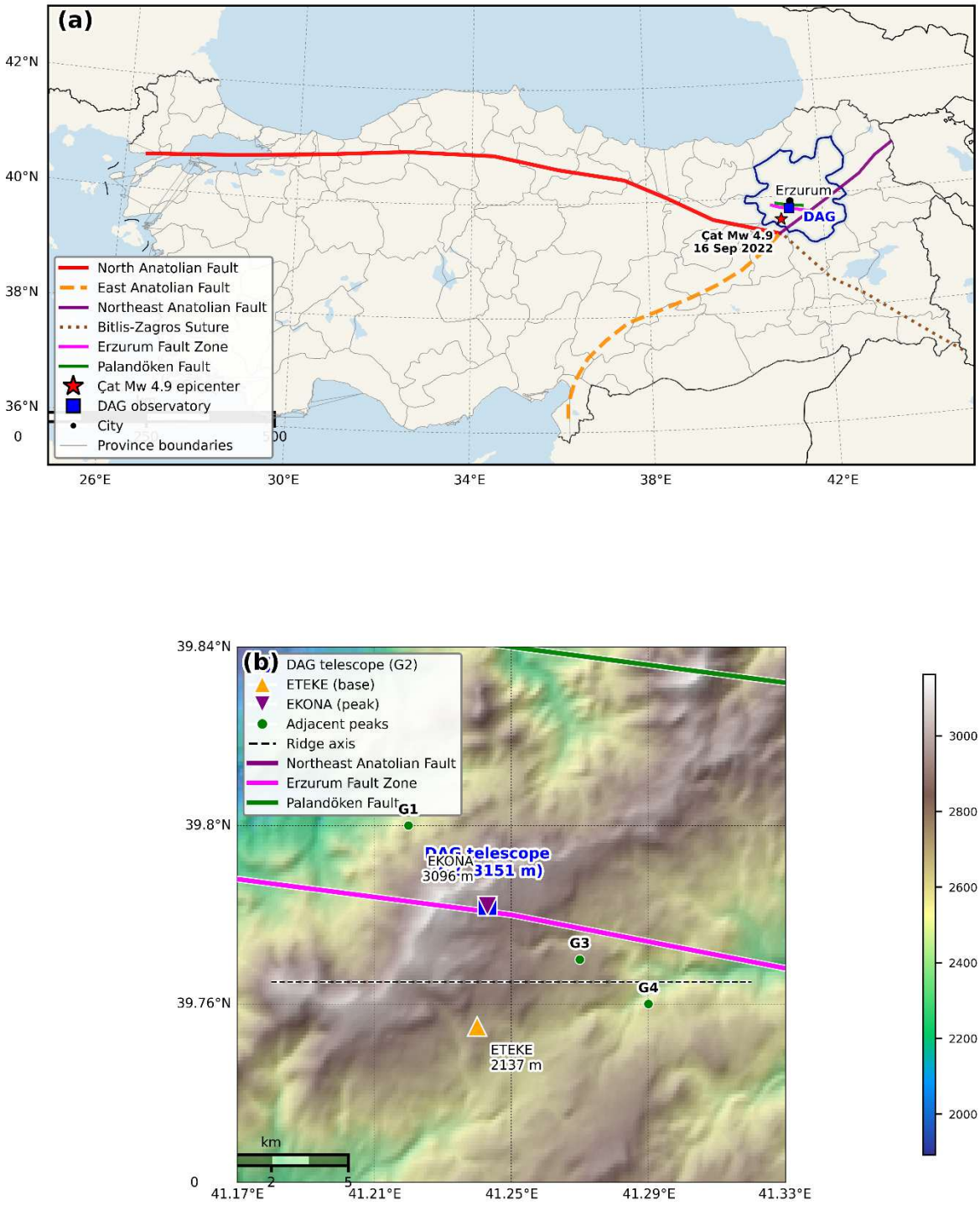


Figure 1. (a) Regional tectonic setting of the Eastern Anatolia Observatory (DAG) showing the North Anatolian Fault (red), East Anatolian Fault (orange dashed), Northeast Anatolian Fault (purple), Bitlis-Zagros Suture (brown dotted), Erzurum Fault Zone (magenta), and Palandöken Fault (green). The Erzurum province is outlined in blue. The 16 September 2022 Mw 4.9 Çat earthquake epicentre (red star), the DAG observatory (blue square), and Erzurum city (black circle) are indicated. **(b)** Local topography of the DAG site from the SRTM 90 m DEM. Triangles mark the two seismic stations ETEKE (base, 2137 m) and EKONA (peak, 3096 m). The blue square marks the DAG telescope on G2 Peak (3151 m). Green dots indicate the undeveloped adjacent peaks G1, G3, and G4. The dashed line shows the approximate ridge axis. Fault traces are simplified after Emre et al. (2013) and Styron & Pagani (2020).



Figure 2. Topographic profile of the DAG site. Generated using Google Earth Pro (Data: Google, Maxar Technologies / Copernicus).

The profile in Figure 2 gives,

- ETEKE elevation: 2137 m
- EKONA elevation: 3096 m
- Horizontal distance between ETEKE and EKONA: 7.87 km
- Maximum slope: 49.1% (26.1°)
- Average slope (lower section): 37.9% (20.8°)
- Average slope (upper section): 19.1% (10.8°)

2.2 Seismic Stations and the Data

The seismic stations ETEKE and EKONA were installed at the DAG site during the observatory's construction period (2012 – 2025) under the supervision of the first author. ETEKE was placed at the mountain base to serve as a reference rock site, while EKONA was installed approximately 55 m below the summit at 3096 m. Every attention was paid to couple the seismometers to the bedrock by forming a sufficiently deep pit. This ensures that the recorded ground motions reflect the bedrock motion. This is essential for a reliable site−response analysis (Pitilakis et al., 2007; Kramer, 1996). Both stations are equipped with Güralp broadband seismometers (Güralp 6-TD) and operate as part of the Turkish National Seismic Network (Ozyazicioglu et al. 2020).

Both stations record three components of ground motion (East, North, Vertical) at a constant sampling rate of 50 Hz. The instrument response was de-convolved to convert velocity recordings in units of nm/s to acceleration in cm/s² using SEISAN software (Ottemöller et al. 2013).

2.3 Seismotectonic and Reference Site Assessment

DAG Observatory is situated in the North-East Anatolian Fault Zone (Figure 1). This is a major strike-slip fault system that accommodates the westward motion of the Anatolian plate. The North Anatolian Fault passes approximately 50 km north of the DAG site, while the East Anatolian Fault lies approximately 60 km south. The local Erzurum Fault Zone and Palandöken Fault lie within 20 kilometres from the observatory (Figure 1a). Seismic activity in the area ranges from moderate to strong, and historical records include earthquakes greater than magnitude 7.0.

The Mw 4.9 Çat earthquake occurred on 16 September 2022 at 20:30:35 local time. The event was located at 39.4111°N, 40.6101°E with a depth of 6.99 km (AFAD). The corresponding epicentral distances were 62.1 km and 66.9 km, and back azimuths of 226.9° and 232.5° for ETEKE and EKONA respectively. The source azimuths at the two stations differ by only 5.6°, which supports the assumption of common source-path effects required by the SSR method. This event provides an ideal dataset for site response analysis for the DAG site. It is close to the site, and high−quality recordings are available at both stations.

The SSR method requires a reference site assumption. This assumption requires that source-path effects are the same at both stations. ETEKE and EKONA are separated by approximately 7.87 km horizontally and 959 m vertically. However, several factors support the validity of this assumption. First, both stations are located on the same mountain massif, and they recorded the same earthquake at similar epicentral distances. Second, two geotechnical investigation reports (Çomaklı, 2012; Kiper, 2013) classify the site as Soil Class A (rock or other rock‑like geological formation) according to EN 1998-5:2004 (European Committee for Standardization, 2004b). The first of these reports (Çomaklı, 2012) gives $V_{s,30}$ = 977 m/s for EKONA vicinity, based on extensive MASW surveys. Third, previous studies have successfully used SSR with similar station separations in mountainous terrain (Spudich et al., 1996; Hartzell et al., 1994; Rovelli et al., 1991; Bouchon & Barker, 1996). We acknowledge that the non-co-location introduces uncertainty. The bootstrap analysis in Section 3.5 quantifies the resampling variability of the record. However, it does not address the bias introduced by the non-co-location of the reference site.

To assess the adequacy of ETEKE as a reference site for the SSR analysis and the potential influence of path effects, we compared the vertical component Fourier amplitude spectra at both stations. The vertical component is generally less affected by site effects, so a near-unity ratio would indicate that path and source effects are comparable. The ratio of vertical spectra (EKONA/ETEKE) is close to unity across the 0.1–20 Hz band, with a mean of 1.05 ± 0.15. However, the ratio exhibits frequency−dependent variation with the exception of the resonance band. At 0.85 Hz, the ratio is 0.34 (SSR_Z = 0.34), indicating significant de−amplification of the vertical component at the peak. This frequency‑dependent variation is expected due to topographic effects and does not invalidate the reference site assumption, as the SSR uses the horizontal components. The near‑unity mean ratio supports the assumption that source-path effects are comparable at the two stations, while the frequency‑dependent variation at 0.85 Hz is consistent with the topographic resonance identified by both the SSR and HVSR methods.

The 7.87 km horizontal separation between ETEKE and EKONA is larger than the typical station spacing used in SSR studies. This introduces two potential biases. First, the source-to-site distance differs by 4.8 km (62.1 km at ETEKE versus 66.9 km at EKONA), so attenuation may not be identical. Using a typical regional attenuation rate for eastern Anatolia (geometric spreading plus inelastic attenuation), a 4.8 km path-length difference translates to an amplitude difference of less than 5% in the 0.5-2 Hz band. Second, the take-off angles to the two stations differ by approximately 6°, which can affect the amplitude of S-wave arrivals by a few percent. The vertical-spectra ratio, which would be near unity if path effects were identical, has a mean of 1.05 ± 0.15 across 0.1-20 Hz. This suggests that the combined path and site bias is of the order of 5-10% on average, though frequency-dependent departures from unity are possible. Without a third station on unmodified bedrock, a rigorous quantification of the residual bias is not possible. The amplification values reported here should therefore be regarded as having an uncertainty of the order of 10% due to reference-site non-co-location.

The direction of the reference-site bias can be estimated from the source geometry. EKONA lies 4.8 km farther from the source than ETEKE (66.9 km versus 62.1 km). Because seismic waves attenuate with distance, the ground motion at EKONA would be systematically smaller than at ETEKE from path effects alone, all other factors being equal. Two attenuation mechanisms contribute at these distances.

Geometric spreading at regional distances scales approximately as 1/R. This gives an EKONA amplitude that is 62.1/66.9 ≈ 0.93 of what it would be at ETEKE. Inelastic damping at 0.85 Hz, with a typical quality factor of Q = 400 (Havskov et al., 2016; Ganbat et al., 2026) and shear-wave velocity of β = 3.5 km/s, gives an additional factor of $\exp(-\pi f \Delta R/\beta Q) \approx 0.99$. The combined effect reduces the EKONA amplitude by approximately 8% relative to ETEKE. This effect works against the observed amplification, not in favour of it. The measured value of 3.89 is therefore a conservative lower bound on the true topographic amplification. Any residual radiation-pattern bias, arising from the 6° back-azimuth difference between the two stations, is expected to be smaller than the systematic distance effect and would not alter this conclusion.

3. Methodology

3.1 Data Processing

Acceleration records from both stations were processed using the following steps:

1. **Instrument correction**: Velocity recordings were converted to acceleration (in Gal) by de-convolving the instrument response using SEISAN software.
2. **Window selection**: The S-wave portion of the record was isolated (10–30 s after P-wave arrival) for spectral analysis (Shearer, 2009). A pre-event noise window (0–8 s) was used for signal-to-noise ratio (SNR) estimation.
3. **Fourier transform**: Smoothed Fourier amplitude spectra were computed using the Konno-Ohmachi algorithm (bandwidth parameter b=20) for both signal and noise windows.
4. **SNR quality control**: Frequencies with SNR < 3.0 were excluded from further analysis.

3.2 Standard Spectral Ratio (SSR) Method

The SSR technique, introduced by Borcherdt (1970), computes the site amplification as the ratio of the Fourier amplitude spectrum at the target site (EKONA) to that at a reference rock site (ETEKE) as given by Equation (1).

$$SSR(f) = \frac{FAS_{EKONA}}{FAS_{ETEKE}} \quad (1)$$

where FAS is the smoothed Fourier amplitude spectrum. The SSR assumes that the source-path effects are similar for both stations due to their proximity, so the ratio isolates the site response at the target site. The geometric mean of the horizontal components was computed by Equation (2).

$$SSR_{GM}(f) = \sqrt{SSR_E(f) \times SSR_N(f)} \quad (2)$$

3.3 Horizontal-to-Vertical Spectral Ratio (HVSR / Nakamura Method)

The HVSR method, popularised by Nakamura (1989), has been extensively reviewed by Lermo and Chávez-García (1993), Fäh et al. (1997), Bard (1999) and Mucciarelli and Gallipoli (2001). This method estimates site response using only a single station, as given by Equation (3).

$$HVSR(f) = \frac{\sqrt{FAS_E(f) \times FAS_N(f)}}{FAS_Z(f)} \quad (3)$$

The method assumes that the vertical component (FAS_Z) is relatively unaffected by site effects, so the ratio amplifies the horizontal-to-vertical resonance. The HVSR provides the fundamental resonance frequency (f_o) at the peak of the HVSR curve and the relative amplification at resonance.

Peaks in the HVSR curve were automatically detected by the scipy.signal.find_peaks function in PYTHON (SciPy v1.10.1). A prominence threshold of 0.3 with no width constraint was used. This is a permissive detection criterion intended to identify all candidate peaks. The significance of each peak was assessed qualitatively in Section 4.3.

While the HVSR method was originally developed for site characterisation in sedimentary basins (Nakamura, 1989), numerous studies have demonstrated its applicability to topographic amplification assessment at rock sites (Chávez-García & Cárdenas-Soto, 2002; Del Gaudio et al., 2008; Pagliaroli et al., 2014). The method relies on the assumption that the vertical component is relatively unaffected by site effects (Fäh et al., 2001). For rock sites with significant topography, this assumption requires verification. In this study, we compare the vertical component spectra at both stations (EKONA and ETEKE) to assess whether the vertical component exhibits significant amplification or de−amplification.

3.4 Seismic Code Comparison

In this section we summarise the provisions in two codes relevant to our study. The relationship between complex site effects and building code provisions has been discussed by Chávez-García and Faccioli (2000) and Dobry et al. (2000).

The Turkish Earthquake Code (AFAD, 2018) uses site amplification factors (F_s / F_1) based on soil classes Z1 – Z4, but does not explicitly address topographic amplification. While the classification accounts for local soil conditions, it is primarily designed for sedimentary site characterisation rather than topographic effects at rock sites. Therefore, the Turkish Earthquake Code-2018 is not included in the comparison. The focus on PS92 and Eurocode 8 is justified because these codes provide explicit topographic amplification factors based on slope geometry, which are directly computable for the DAG site. The topographic amplification provisions of these two seismic codes are summarised below.

PS92 (NF P06-013, 1995):

- Based on slope geometry using upstream slope (i) and downstream slope (I).
- $\tau = 1.0$ if $(I – i) < 0.40$
- $\tau = 1.0 + 0.80 \times (I – i – 0.40)$ if $0.40 \leq (I – i) \leq 0.90$
- $\tau = 1.4$ if $(I – i) > 0.90$

Eurocode 8 (EN 1998‑5:2004, Annex A):

In Eurocode 8, the elastic response spectrum for the site is defined according to EN 1998-1:2004 *(*European Committee for Standardization, 2004a*).* The average slope along the entire profile is 12.9°. The local slope at the peak (Figure 2) reaches 26.1° (49.1%).

Eurocode 8 Part 5 (EN 1998-5:2004) Annex A provides simplified topographic amplification factors S_t, which are period-independent multipliers on the elastic design response spectrum. These factors are applicable to two-dimensional topographic irregularities such as long ridges and cliffs higher than about 30 m. Annex A states that for average slope angles below about 15° topographic effects may be neglected, but recommends a specific study where the local topography is strongly irregular. For steeper terrain, it distinguishes between (a) isolated cliffs and slopes, for which $S_t \geq 1.2$ applies near the top edge, and (b) ridges whose crest width is significantly less than their base width, for which $S_t \geq 1.4$ applies for average slopes greater than 30° and $S_t \geq 1.2$ for smaller average slopes.

The DAG crest is a ridge-type feature with a crest width significantly smaller than its base width. The average slope along the ETEKE-EKONA profile is 12.9°, while the maximum local slope at the crest reaches 26.1°. Although the average slope is below the 15° threshold, the local irregularity of the crest places the site in the "strongly irregular local topography" case. For this case Annex A recommends a specific study. The ridge provision (b) for an average slope below 30° gives $S_t \geq 1.2$. We therefore adopt

the Annex-consistent minimum value of S_t = 1.2 for comparison with the empirical amplification. We note that applying the strict average-slope criterion would yield S_t = 1.0. The adopted value is thus conservative with respect to the code.

From the Google Earth profile, the upstream slope (i) = 0.20 (upper section), downstream slope (I) = 0.35 (lower section), maximum slope = 26.1°, and average slope = 12.9°, the amplification factors are given in Table 1.

Table 1. Summary of code parameters and topographic amplification factors.

Code	Parameter	Value	Result	Factor
PS92	Upstream slope (i)	0.20	I–i = 0.15 < 0.40	τ = 1.00
PS92	Downstream slope (I)	0.35	-	
EC8	Average slope	12.9°	-	S_t = 1.2
EC8	Local Maximum slope	26.1°	Ridge provision (b), strongly irregular topography	$S_t \geq 1.2$

The maximum slope of 26.1° would suggest a significant topographic effect, yet the PS92 factor (τ = 1.0) and the Eurocode 8 factor (S_t = 1.2) yield relatively low amplification factors. The reason for this discrepancy is that the PS92 factor is based on the difference between upstream and downstream slopes (I–i = 0.15), which is less than the 0.40 threshold.

3.5 Uncertainty Quantification

The bootstrap resampling procedure follows the general framework of Efron and Tibshirani (1993). To assess the robustness of the Fourier SSR estimates, two structure-preserving resampling schemes were applied. First, a sub-window ensemble bootstrap divided the 20 s S-wave window into two non-overlapping 10 s sub-windows, computed the SSR for each, and resampled the ensemble 1000 times with replacement. Second, a moving block bootstrap (Künsch, 1989) resampled the full S-wave series in blocks of 4 s (200 samples at 50 Hz), preserving short-range phase coherence within each block. The moving-block length (4 s) was chosen to span at least two cycles of the lowest frequency of interest, 0.5 Hz. Frequencies below 0.5 Hz are not reliably resolved by the 20 s S-wave window and are therefore not interpreted in this work.

Both methods yield a bootstrap distribution of the SSR at each frequency. The median, 5th percentile, and 95th percentile were computed to provide a best estimate and a 90% confidence interval.

A key methodological consideration applies to narrow-band spectral features. The 0.85 Hz topographic resonance has a bandwidth of roughly 0.1-0.2 Hz. To resolve a spectral peak of this width, a time window of at least 5-10 s is required. Resampling schemes that break the record into shorter segments, such as sub-window division or block resampling reduce the frequency resolution, which smear the peak. As a result, the bootstrap medians computed for the narrow-band Fourier SSR should be regarded as conservative lower bounds on the actual amplification. The full-window point estimate of SSR_{GM} = 3.89 at 0.85 Hz should be treated as an upper estimate of the narrow-band amplification. The bootstrap median of 2.06 provides a conservative lower bound. A robust point estimate cannot be determined from a single 20 s window.

To quantify the uncertainty estimate for the amplification relevant to engineering design, the PSA ratio at T = 1.18 s was also subjected to the same moving block bootstrap procedure. Since PSA is obtained by integrating the SDOF oscillator with 5% damping over a range of frequencies, it is not affected by the narrow-band smearing problem. The bootstrap median for PSA comes out to be 1.80, matching the point estimate exactly, and the 90% confidence interval spans [1.15, 2.73]. The lower confidence limit lies above unity, which confirms that the broadband amplification at the resonance period is statistically robust.

All bootstrap computations were repeated with n = 500 and n= 1000 resamples. n=1000 was found to be adequate for obtaining stable percentile estimates.

4. Results

4.1 Time Histories

Figure 3 shows the acceleration time histories of both stations for all three components. The 10 - 30 s S-wave window and the 0 - 8 s noise window are highlighted. The peak ground accelerations (PGA) for the N-components were approximately 1.5 Gal at EKONA and 1.4 Gal at ETEKE.

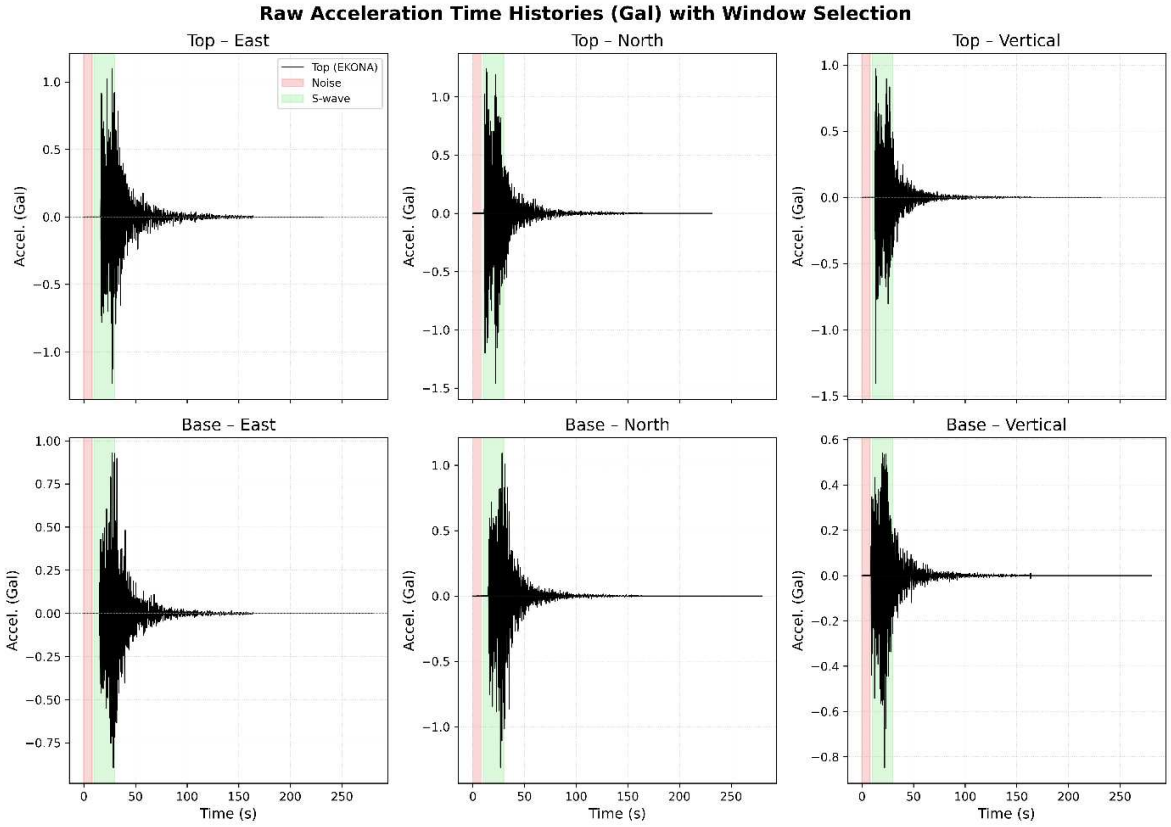


Figure 3. Acceleration time histories for EKONA and ETEKE stations. The red shaded region designates the noise and the green shade indicates the S-wave windows.

4.2 Fourier Amplitude Spectra

Figure 4 shows the signal and noise spectra, and SNR for both stations. The individual Fourier amplitude spectra and corresponding HVSR curves for each station are provided in Figures A1 and A2 in the Appendix. Similar spectral separation has been documented by Field and Jacob (1995).

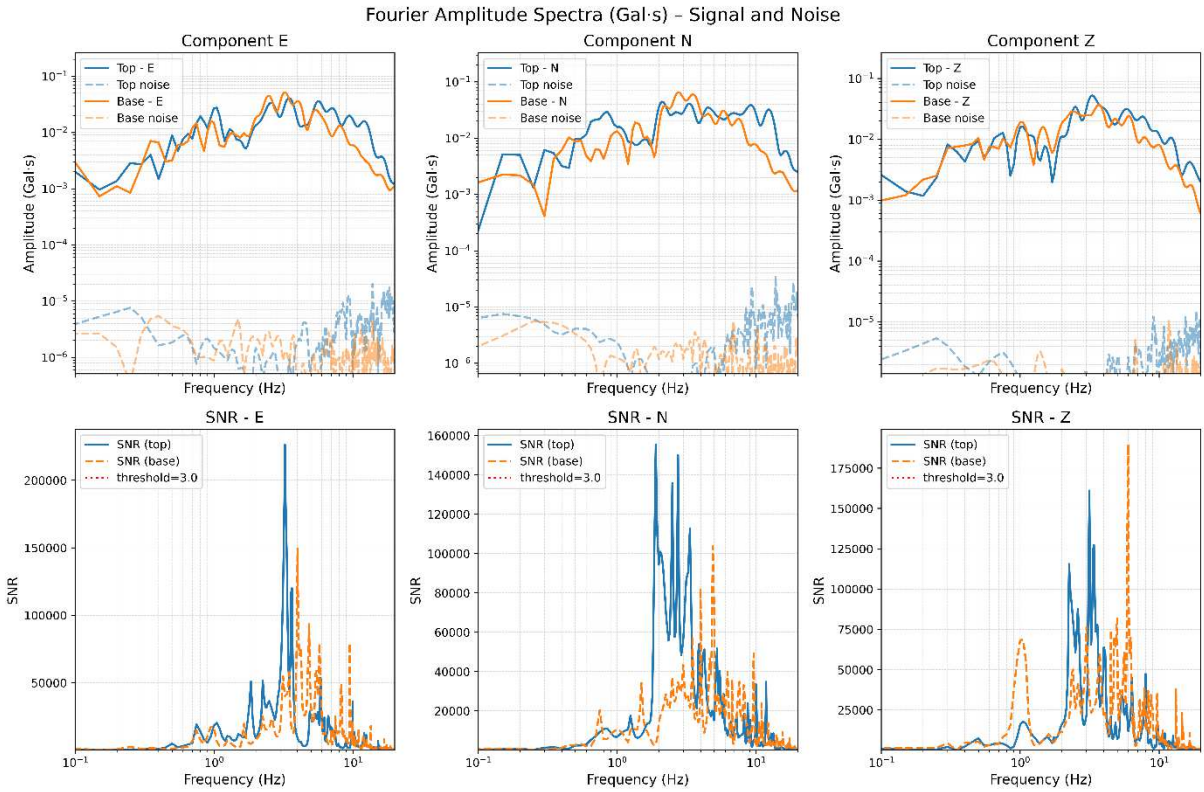


Figure 4. Smoothed Fourier amplitude spectra (top row) for EKONA (blue) and ETEKE (orange) stations. Dashed lines show noise spectra. SNR (bottom row) exceeds 3 in the 0.1-20 Hz band.

The spectra in Figure 4 indicate that

- Higher amplitudes at EKONA compared to ETEKE across most frequencies. This pattern is consistent with Borcherdt and Gibbs (1976).
- Clear separation between signal and noise (SNR > 3) across the 0.1–20 Hz band.
- Distinct spectral features, particularly around 0.85 Hz, suggesting topographic resonance.

4.3 HVSR Results

Figure 5 gives a comparison of the HVSR curves for EKONA and ETEKE stations. Because both stations rest on bedrock, the likelihood of local sedimentary resonance is minimised. At EKONA, the HVSR curve shows a pronounced peak at 0.85 Hz with an amplitude of 10.11. This peak does not appear in ETEKE curve, which confirms that this resonance peak is topographically induced. Secondary peaks at 1.60 Hz and 2.25 Hz also occur at EKONA. These can be attributed to the higher resonant modes of the crest. Meanwhile, the HVSR curve for ETEKE displays peaks at 0.55 Hz and 1.30 Hz. These represent the local geological features or the dynamic response of the mountain base.

The fundamental frequency of 0.85 Hz is the key parameter for seismic design. Structures with periods near this value will experience amplified shaking.

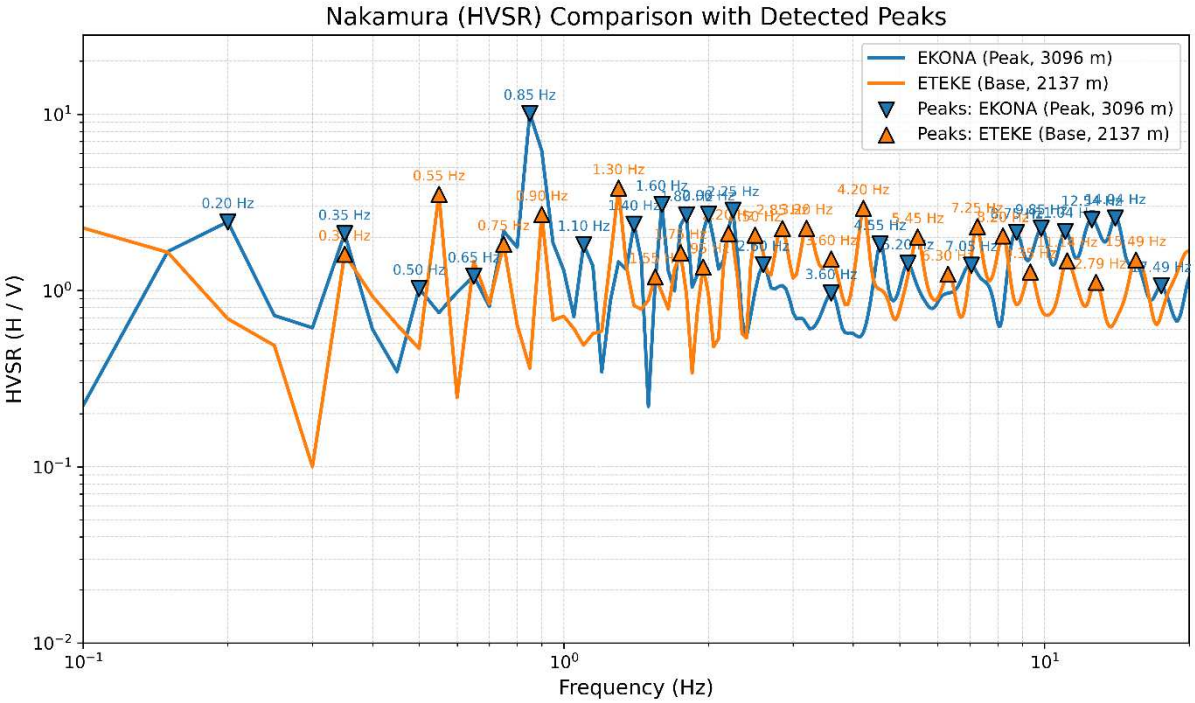


Figure 5. Horizontal-to-Vertical Spectral Ratio (HVSR) curves for EKONA (blue) and ETEKE (orange). The fundamental resonance at EKONA at 0.85 Hz is clearly visible (Nakamura, 1989).

The small vertical component at EKONA substantially amplifies the HVSR ratio. This results in the high amplitude of 10.11 (Figure A1 in the appendix). Although this is consistent with topographic focusing, the amplitude needs interpretation. High HVSR amplitudes at rock sites can also arise from other effects. These include directional amplification of the horizontal components, as well as de–amplification of the vertical component. Diffraction at sharp topographic features can also contribute (Del Gaudio et al., 2008; Pagliaroli et al., 2014). The $SSR_Z = 0.34$ provides direct evidence that vertical de–amplification contributes to the high HVSR amplitude. This validates the interpretation above.

Table 2 summarises the HVSR peak frequencies and amplitudes. The dominant peak at 0.85 Hz in EKONA is the fundamental frequency of the crest. This resonance is absent at the base station. This confirms the topographic origin of amplification. The high HVSR amplitude indicates very strong horizontal-to-vertical amplification that significantly exceeds typical values (1–4) observed at sedimentary sites.

Table 2. HVSR peak frequencies and amplitudes for EKONA and ETEKE stations.

Station	Elevation (m)	Peak Frequency (Hz)	Peak Amplitude (HVSR)	Interpretation
EKONA (Peak)	3096	**0.85**	**10.11**	**Fundamental topographic resonance**
EKONA (Peak)	3096	0.20	2.45	Low-frequency peak, not reliably resolved in a 20 s window
EKONA (Peak)	3096	1.60	3.08	Higher-mode topographic resonance
EKONA (Peak)	3096	2.25	2.86	Higher-mode topographic resonance
ETEKE (Base)	2137	0.55	3.52	Local soil/rock resonance
ETEKE (Base)	2137	1.30	3.82	Higher-mode resonance
ETEKE (Base)	2137	4.20	2.93	Higher-mode resonance

HVSR amplitudes are ratios of horizontal to vertical motion and should not be interpreted as amplification factors.

The 0.20 Hz peak is near the resolution limit of a 20 s window, therefore it is not discussed here. The HVSR amplitude of 10.11 should not be interpreted as an amplification factor. It is a horizontal-to-vertical ratio, which is influenced by both horizontal amplification and vertical de-amplification. The SSR value of 3.89 at the same frequency is the appropriate amplification metric.

Figure 6 gives an H/V plot from an independent ambient noise measurement in one of the site investigation reports of DAG site (Çomaklı, 2012). This figure also displays the fundamental resonant frequency at 0.90 Hz. Its relation to validation of fundamental resonant frequency is discussed in section 5.1.

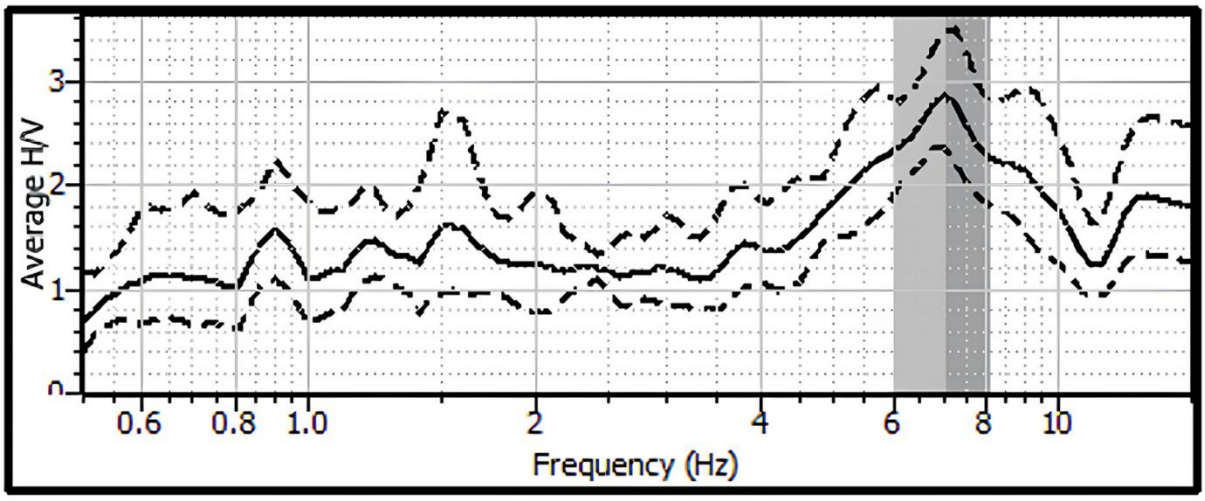


Figure 6. H/V based on ambient noise measurement at EKONA (Çomaklı, 2012, used with permission).

4.4 SSR Results

Figure 7 presents the SSR amplification curves for all components and the geometric mean. The SSR_{GM} shows a clear peak of 3.89 at 0.85 Hz. This is in direct agreement with the HVSR resonant frequency. The North component shows the largest amplification of 4.52 at 0.85 Hz. The PS92 factor of $\tau = 1.0$ and Eurocode 8 factor of $S_t = 1.2$ are also plotted for comparison.

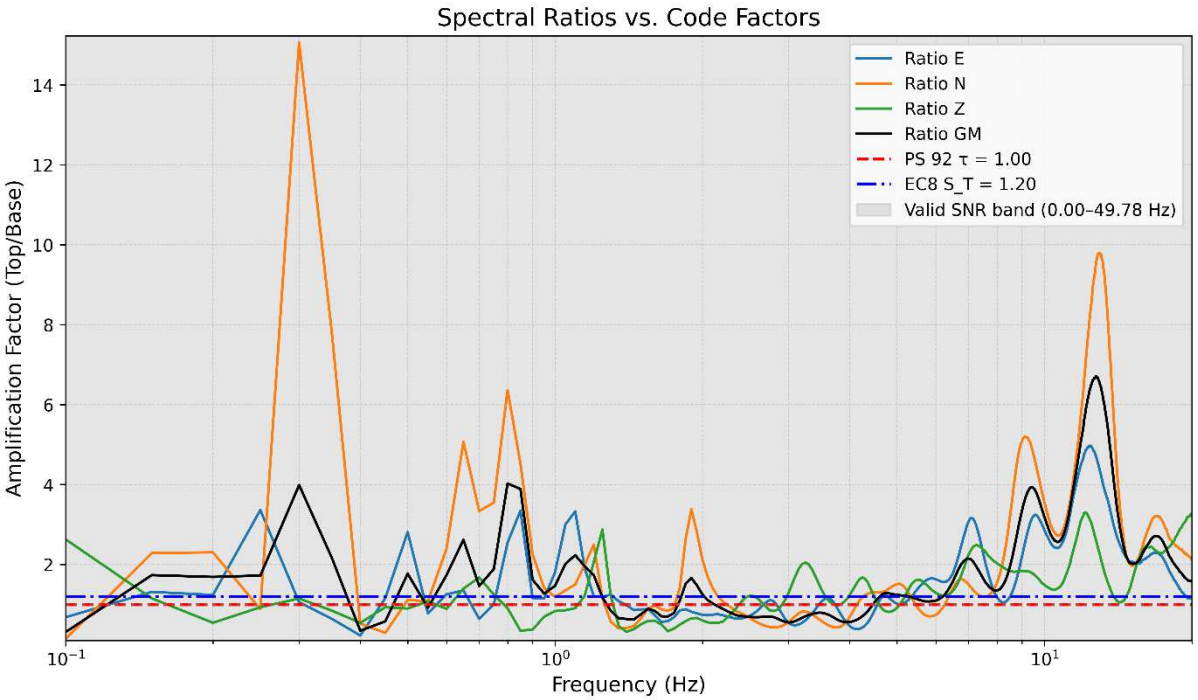


Figure 7. SSR amplification curves for each component motion and the geometric mean. SSR_{GM}=3.89 at 0.85 Hz is the fundamental resonance, where N-component peaks at 4.52. Horizontal lines show the code factors.

Table 3 summarises the SSR amplification factors at typical frequencies.

Table 3. SSR amplification factors for all components and the geometric mean.

Frequency (Hz)	**Period (s)**	**SSR_E**	**SSR_N**	**SSR_Z**	**SSR_{GM}**	**Interpretation**
0.85	1.18	**3.35**	**4.52**	0.34	**3.89**	**Fundamental topographic resonance**
0.20	5.00	1.24	2.30	0.54	1.69	Low-frequency amplification
1.60	0.63	0.72	0.97	0.59	0.84	No amplification (de-amplification)
2.00	0.50	0.74	2.13	0.60	1.26	Moderate N-component amplification
5.00	0.20	1.02	1.52	0.92	1.24	Near unity
10.00	0.10	2.86	3.55	1.49	3.19	High-frequency amplification

The SSR_N value of 15.06 at 0.30 Hz is not listed in the table. It is an isolated outlier that corresponds to a local spectral minimum at ETEKE. The SNR at this frequency is close to the 3.0 threshold, and the estimate should not be interpreted as a site resonance.

The SSR analysis confirms the topographic resonance at 0.85 Hz with a geometric mean amplification of 3.89. Component-level values are 3.35 (E) and 4.52 (N), the latter being the largest amplification observed at any frequency (Table 3). The directional character of this response is interpreted in Section 5.2 in light of the source geometry.

Statistically meaningful uncertainty estimates were obtained by applying moving block bootstrap to the PSA ratio at T = 1.18 s (Figure 8). The resulting GM median of 1.80 matches the point estimate. The 90% confidence interval of [1.15, 2.73] remains entirely above unity. This demonstrates that the observed broadband amplification is statistically significant.

The Fourier SSR bootstrap (Figure 9) produces conservative lower bounds with a MBB median of 2.06 at 0.85 Hz. Both resampling schemes shorten the effective time window, which degrades frequency resolution and smears the narrow-band peak. Therefore, the full-window point estimate of SSR_{GM} = 3.89 should be treated as an upper estimate of narrow-band amplification. A robust point estimate for the narrow-band Fourier SSR at 0.85 Hz cannot be determined from a single 20 s window. This behaviour reflects a fundamental property of bootstrap methods applied to narrow-band features, rather than a numerical artefact.

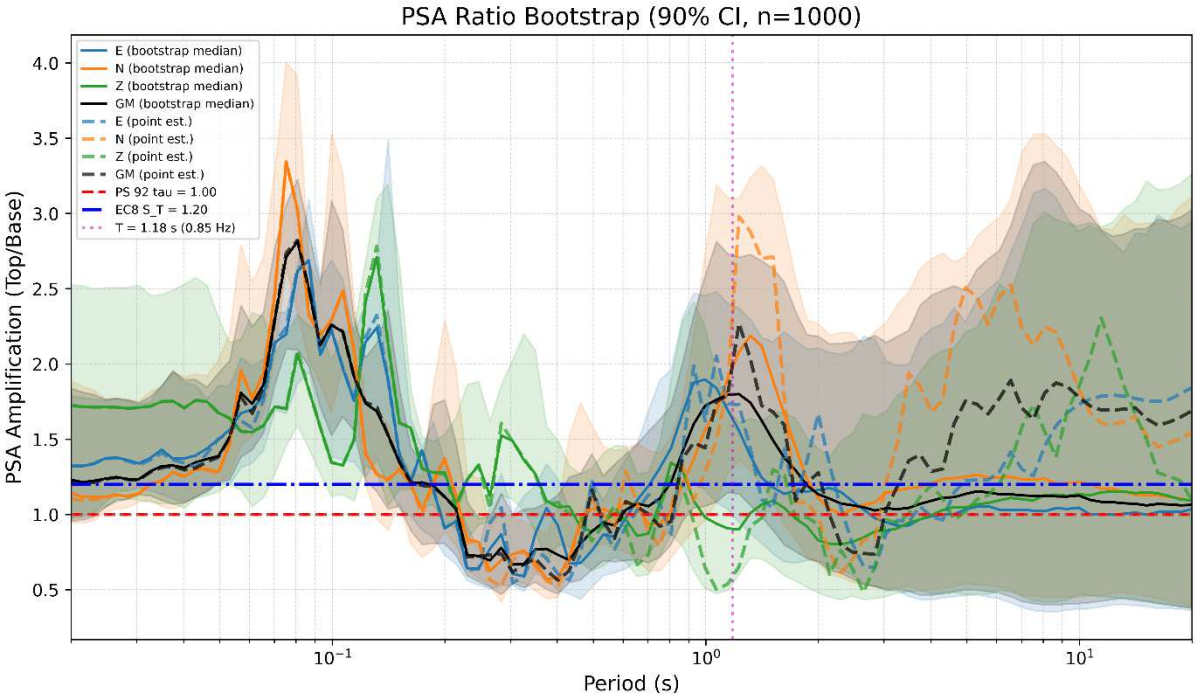


Figure 8. Bootstrap PSA medians and 90% confidence bands obtained by moving-block resampling of the S-wave (n = 1000, 5th-95th percentiles shaded).

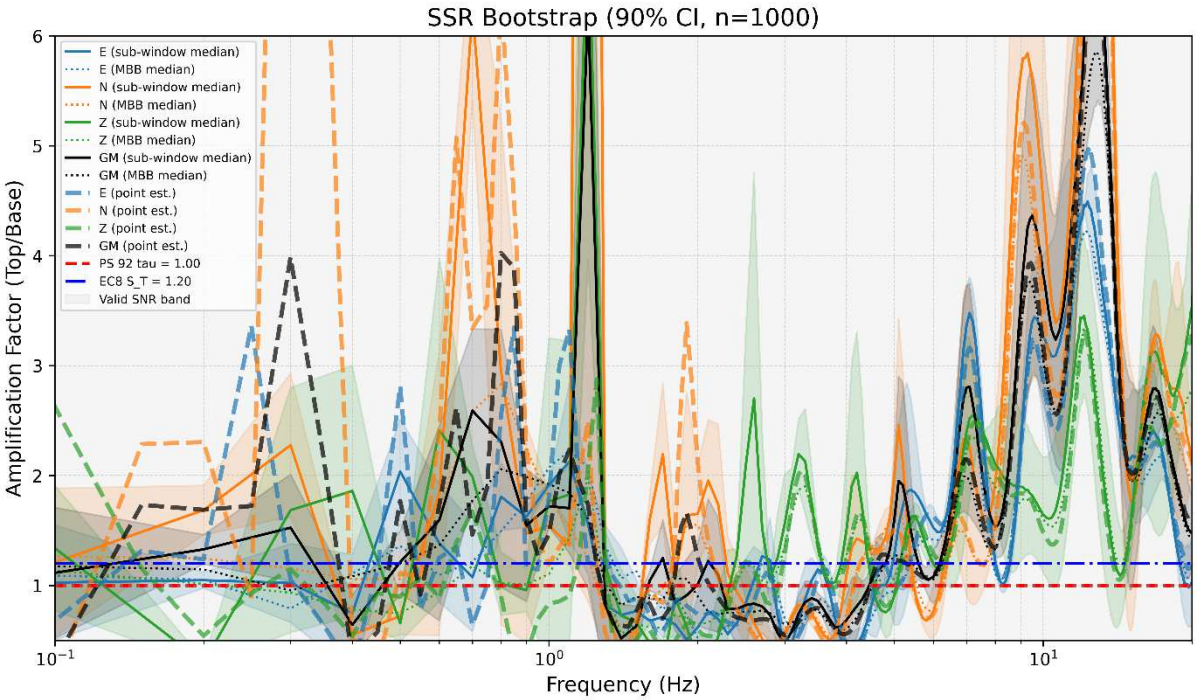


Figure 9. Bootstrap SSR medians and 90% confidence bands (n = 1000, 5th-95th percentiles). The moving-block bootstrap yields conservative lower bounds (median 2.06 at 0.85 Hz) because the resampling schemes reduce the effective frequency resolution and smear the narrow-band peak. The full-window point estimate of SSR_GM = 3.89 is treated as an upper estimate, and the bootstrap median of 2.06 as a conservative lower bound.

4.5 Pseudo-Acceleration Response Spectra

Figure 10 presents the 5% damped PSA for the two stations. EKONA, the peak station, exhibits higher spectral accelerations at periods below 2 s. The base station ETEKE, however, shows higher amplitudes at longer periods between 3 and 5 s. This pattern indicates that the mountain amplifies high−frequency motion, with the strongest topographic effect occurring at the fundamental frequency of 0.85 Hz.

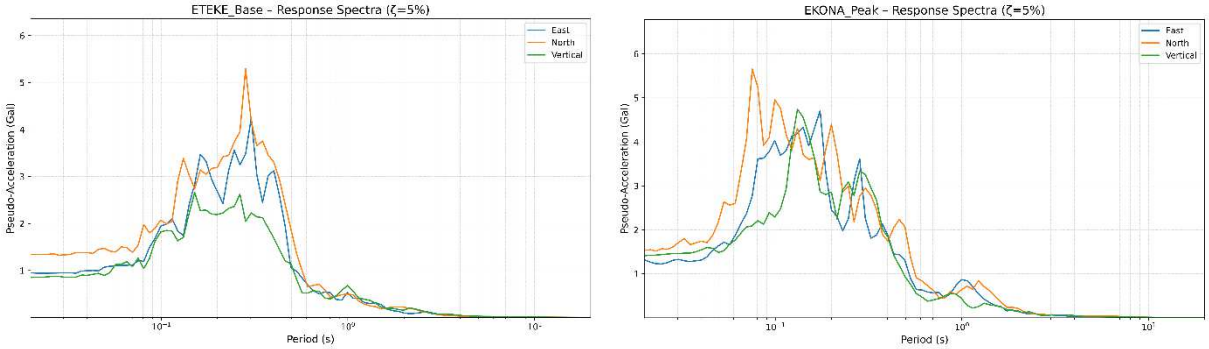


Figure 10. Pseudo-acceleration response spectra for ETEKE (left) and EKONA (right) stations.

Table 4 summarises the PSA values at key periods.

Table 4. PSA values at key periods for both stations.

Period (s)	PSA Ratio, E	PSA Ratio, N	PSA Ratio, GM	Interpretation
0.02 (PGA)	1.32	1.10	1.21	Near Unity
1.18 (0.85 Hz)	1.73	1.86	**1.80**	**Fundamental topographic resonance**
1.227 (0.815 Hz)	1.73	2.98	**2.27**	**PSA local peak**
2.00	1.67	0.98	1.28	Moderate amplification
4.00	0.98	1.68	1.29	Moderate amplification

The peak-to-base PSA ratio varies strongly with frequency. At T = 0.02 s, corresponding to PGA, the ratio is 1.21. The PSA ratio reaches a maximum of 2.27 at T=1.227 s (0.815 Hz). At the SSR resonance period of 1.18 s the GM ratio is 1.80 (Figure 11). The slight difference between the PSA peak period T=1.227s and SSR/HVSR resonance period T=1.18 s arise from the damped PSA response. At any rate, this result confirms the topographic resonance identified by the SSR and HVSR methods. The amplification persists at longer periods as well, such as 1.28 at T = 2.00 s and 1.29 at T = 4.00 s. This indicates that topographic effect at the peak remains significant across a broad range of periods.

4.6 Comparison with Seismic Codes

This section compares the empirical amplification at the DAG site with the topographic amplification provisions of PS92 and Eurocode 8. The methodology for developing site-dependent design spectra was established by Borcherdt (1994). His work provides the basis for the site coefficients used in modern building codes.

The empirical amplification at the DAG site is frequency-dependent (Figure 11). The PSA ratio reaches 1.80 at T = 1.18 s and 2.27 at T = 1.227 s (Table 4). The code-prescribed topographic factors, by contrast, are frequency-independent scalar multipliers applied to the entire design response spectrum. A direct numerical comparison between a frequency-dependent spectral ratio and a frequency-independent code factor is therefore not valid at a single period.

The code−prescribed topographic amplification factors are summarised in Table 5. PS92 gives τ = 1.00 for this site. This is based on the slope geometry (I − i = 0.15), which falls below the 0.40 threshold. Eurocode 8 classifies the site as a ridge-type feature with strong local irregularity. Following the ridge provision for average slopes below 30°, we adopt the minimum value of S_t = 1.2 for comparison.

Table 5. Comparison of PSA amplification at 0.85 Hz with code prescribed topographic factors.

Period (frequency)	**Maximum Code Factor (PS92 and EC8)**	**Empirical PSA Ratio**	**PSA Ratio/Code Factor**
T=1.18 s (0.85 Hz)	1.4	**1.80**	**1.28**
T=1.227 s (0.815 Hz)	1.4	**2.27**	**1.62**

The last column is shown for reference only and does not represent a code exceedance factor.

To place the empirical results in context, we consider the following three questions.

Does the code factor envelope the empirical amplification across the period range of interest? This is the correct basis for evaluating code conservatism and requires the site-specific uniform hazard spectrum. This spectrum should be amplified by the frequency-dependent function of Figure 11, and compared to the code-based design spectrum. This full spectral comparison is recommended for future work once additional records are available to constrain the amplification function.

Does the code factor capture the peak empirical amplification in the resonance band? The peak PSA ratio of 2.27 at T = 1.227 s exceeds the maximum code-prescribed factor of 1.4 by 62%. Even the resonance-period value of 1.80 at T = 1.18 s exceeds it by 28%. This observation suggests that the code topographic factors may be insufficient for this steep ridge. Nevertheless, the finding is based on a single event at one azimuth and should be treated as preliminary.

Can the Fourier SSR be compared to the code factors? No. The SSR measures narrow-band Fourier amplification at a single frequency. The code factors, however, are intended to scale the broadband response spectrum. The SSR_{GM} value of 3.89 at 0.85 Hz is reported as a site-characterisation result, not as a code exceedance factor. Therefore, the PSA ratio of 1.80 is the appropriate engineering metric for comparison.

In summary, the empirical amplification at the resonance band exceeds the maximum code factors at the DAG site. Because the comparison relies on a single event, the finding is presented as a preliminary observation that motivates further study. It is not a generalizable conclusion about the adequacy of code provisions.

Figure 11 illustrates the PSA ratio curves with the code factors. The narrow-band peak at 0.85 Hz is clearly seen.

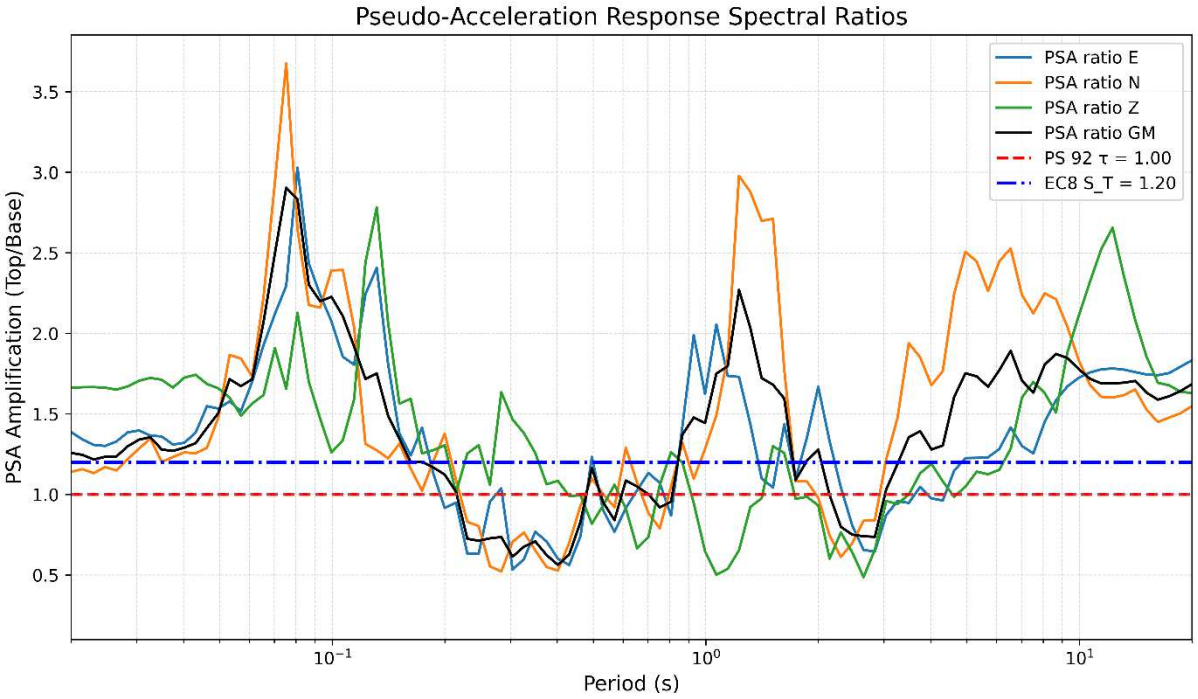


Figure 11. PSA ratio versus code factors. The empirical PSA amplification of 1.80 at T = 1.18 s exceeds the maximum code-prescribed factor of 1.40 by 28%. The narrow-band Fourier SSR of 3.89 at 0.85 Hz is also shown.

5. Discussion

5.1 Cross-Validation of SSR and HVSR Methods

The two methods, SSR and HVSR, identify 0.85 Hz as the fundamental resonant frequency. Since both methods use the same horizontal-component spectra, this agreement is expected and cannot be treated as an independent confirmation.

Instead, confidence in the 0.85 Hz resonance rests on three lines of evidence, which do not share this dependence. First, the 0.85 Hz peak is absent at the base station ETEKE (Figure 5). This points to a topographic effect localised at the crest. Second, the 5% damped response spectra show a broadband amplification near the corresponding resonance period (Figure 10). Third, an independent ambient-noise survey around the crest (Çomaklı, 2012; Figure 6) shows a clear H/V peak at ~0.90 Hz. This survey was conducted ten years before the Çat earthquake with different instrumentation. The 6% difference between 0.85 Hz and 0.90 Hz is within the variability expected from measurement location, methodology, and site conditions. These independent observations together establish the fundamental resonance band of the site.

The HVSR method assumes that the vertical component is relatively unaffected by site effects. The ratio of vertical-component Fourier spectra (EKONA/ETEKE) is close to unity across the 0.1-20 Hz band. As seen from Figure 4, the mean ratio is 1.05 ± 0.15. Therefore, the assumption holds for this rock site on average across the analysed band. This provides additional support for the HVSR results. There is, however, one notable exception. At the 0.85 Hz resonance, the ratio drops to 0.34.

The HVSR method was developed for sedimentary basins (Nakamura, 1989). However, recent studies have validated its use for topographic amplification (Del Gaudio et al., 2008; Pagliaroli et al., 2014). EKONA shows a high HVSR amplitude. This is consistent with strong topographic focusing. Similar observations exist at other mountain peaks (Zaslavsky et al., 2000).

The high HVSR amplitude of 10.11 at 0.85 Hz requires interpretation. While this value is consistent with topographic focusing, it is substantially higher than the typical HVSR amplitudes of 3 to 5 observed at other mountain crests (Zaslavsky et al., 2000). The high amplitude is primarily the result of de−amplification in the vertical component at the crest (SSR_Z = 0.34 at 0.85 Hz). This further amplifies the HVSR ratio. This vertical de−amplification may be caused by wave−conversion at the topographic feature, like P−wave to Rayleigh−wave conversion or by diffraction at the sharp crest (Geli et al., 1988; Paolucci, 2002). The SSR analysis confirms that the horizontal amplification is substantial ($SSR_{H, GM}$ = 3.89 at 0.85 Hz). However, it is not as high as the HVSR amplitude suggests. Therefore, the HVSR amplitude of 10.11 should be interpreted as a relative measure rather than an absolute amplification factor. These results are summarised in Table 6.

Table 6. Comparison of SSR and HVSR amplification at 0.85 Hz.

Frequency (Hz)	$SSR_{H,GM}$	SSR_Z	HVSR (EKONA)	HVSR (ETEKE)
0.85	3.89	0.34	10.11	1.82

HVSR amplitudes are ratios of horizontal to vertical motion and should not be interpreted as amplification factors.

These results confirm that the observed resonance is a real topographic effect, and not an artefact of the methods. Although SSR and HVSR can differ in absolute amplification values, they generally agree on the resonant frequency (Zaslavsky et al., 2000; Geli et al., 1988; Paolucci, 2002).

The discrepancy in the values is expected. HVSR measures horizontal-to-vertical spectral ratio, whereas SSR gives the absolute amplification relative to a reference site. Since the vertical component at the peak is relatively de-amplified, the HVSR amplitude is often higher.

The high HVSR at the EKONA points to strong topographic amplification. However, HVSR is not an amplification factor. It reflects the ratio of horizontal to vertical motion. The SSR value of 3.89 at 0.85 Hz is the appropriate amplification metric for the site. Since the site rests on competent rock with no appreciable soil cover, the amplification does not arise from sedimentary resonance. Similar high HVSR amplitudes have also been reported at mountain tops by Zaslavsky et al. (2000) and Del Gaudio et al. (2008).

Because these findings rely on a single earthquake, uncertainty quantification is essential. To this end, the PSA bootstrap analysis establishes robust statistical bounds. The point estimate of 1.80 lies well within the 90% confidence interval of [1.15, 2.73]. Since the lower bound remains above unity, the observed amplification is a genuine physical phenomenon rather than a stochastic artefact.

For the narrow-band Fourier SSR, the MBB bootstrap median is 2.06. This represents a conservative lower bound on the amplification. All resampling schemes that shortens the effective time window smear the sharp 0.85 Hz peak. The full-window point estimate of SSR_{GM} = 3.89 is the value obtained from the entire 20 s S-wave window. Because the 0.85 Hz resonance has a bandwidth of only 0.1-0.2 Hz, this point estimate is sensitive to the selected window size. It should be treated as an upper bound estimate of narrow-band amplification. The bootstrap median of 2.06 provides a lower bound. The true amplification lies between these two bounds.

In short, while the SSR and HVSR results align, the shared horizontal component prevents true statistical independence. We therefore treat their agreement as supportive rather than confirmatory. Confidence in 0.85 Hz resonance relies on three independent observations. These are the absence of a peak at the reference station, the consistency of the PSA spectra, and the independent ambient-noise measurement.

5.2 Physical Mechanism of Topographic Amplification

The observed resonance occurs at 0.85 Hz (T = 1.18 s). The wavelength that corresponds to this frequency is comparable to the dimensions of the mountain. With an average shear−wave velocity of 977 m/s for the bedrock of DAG site (Çomaklı, 2012), the wavelength at 0.85 Hz is about $\lambda = Vs/f = 977/0.85 \approx 1.15$ km. This length is on the order of the mountain's approximate width of 1.5 km and height of 1.0 km. It also satisfies the theoretical criterion that topographic amplification depends mainly on relief geometry in wavelength scale (Geli et al., 1988; Fäh et al., 2001; Paolucci, 2002; Pitilakis et al., 2007).

The ridge axis exhibits two distinct orientation scales. Across the entire 70 km extent of the Palandöken range, the trend is approximately east-west with a regional azimuth of 78°. This azimuth is extracted from the SRTM 90 m DEM (Jarvis et al., 2008) using a best-fit line through the highest crests. Restricting the fit to a local 16 km × 12 km window centred on the observatory shifts the ridge azimuth to 58.5°. This shift indicates that the ridge deflects toward the northeast near the observatory. This local change in orientation is important because topographic amplification is governed by the slope geometry at the scale of the incident wavelength, rather than the regional trend.

The horizontal-component amplification at 0.85 Hz is stronger on the North component ($SSR_N = 4.52$) than on the East component ($SSR_E = 3.35$). Interpreting this contrast requires consideration of the source geometry. The epicentre lies to the southwest of the site with back azimuths of 226.9° at ETEKE and 232.5° at EKONA (measured clockwise from North at the station, pointing toward the source). The wave-propagation direction (back-azimuth minus 180°) is therefore approximately 47° at ETEKE and 53° at EKONA. Both values differ from the local ridge azimuth of 58.5° by less than 12°. Thus the incoming S wave ray-paths propagate nearly parallel to the local ridge axis. The stronger North-component response is therefore not aligned with either the ridge-normal or the transverse direction, and cannot be attributed to the asymmetric slope geometry on the basis of this single event. Three effects are likely superimposed. (i) Because the ray path is nearly parallel to the local ridge axis (less than 12°), the incoming wavefield interacts with the ridge primarily in the along-ridge direction. For a strike-slip source, the dominant S-wave polarization is horizontal and perpendicular to the ray path. In this near-along-ridge geometry, SH polarization is oriented at roughly 137° from North, which is close to the ridge-normal direction of 148.5°. Ridge-normal SH motion projects approximately 73% onto the North component and 68% onto the East component. Therefore, the observed North-component dominance is at least qualitatively consistent with near-axial propagation of SH motion. (ii) The structural asymmetry of the mountain, whose steeper western slope can focus energy arriving from the southwest. (iii) The local ridge orientation at the observatory (58.5° from North), which is oblique to the regional trend (78°), so the relationship between the incoming wavefield and the local topographic feature depends on which scale dominates the response. Directional topographic site response of this kind has been documented at comparable ridge sites (Spudich et al., 1996). Because only one source azimuth is available here, the relative contributions of these effects cannot be separated. Therefore, recordings from events at complementary azimuths will be needed to establish whether the North-component dominance is a stable feature of the site.

The amplification observed at around 10 Hz ($SSR_E = 2.86$, $SSR_N = 3.55$) is likely associated with near-surface weathering or small−scale topographic features rather than the mountain−scale resonance. Similar high−frequency amplifications have been observed at rock sites with shallow weathering layers (e.g., Steidl et al., 1996; Field & Jacob, 1995).

5.3 Implications for Seismic Design

The amplification factors derived in this study are intended to complement the probabilistic seismic hazard assessment of Özyazıcıoğlu et al. (2024). While the previous hazard study provided the regional hazard levels, the present work provides the site−specific, frequency−dependent topographic amplification that must be applied to those spectra for the seismic design of the DAG telescope. Implications for the DAG telescope and future installations include:

1. Broadband amplification. The PSA ratio at T=1.18 s is 1.80, which exceeds the maximum code-prescribed factor of 1.4. The peak PSA ratio of 2.27 at T = 1.227 s exceeds the same factor by a larger margin. These observations suggest that the code factors may be unconservative for this steep ridge. However, this result is based on a single event, hence should be treated as preliminary.

2. Site-specific design spectra. The frequency-dependent amplification function in Figure 11 should be applied to the design spectrum in the code or uniform hazard spectrum in Ozyazıcıoglu et al. (2024). This will produce site-specific design spectra for the DAG site. Particular attention should be given to the 0.8–1.5 s period range. This approach follows the methodology of Borcherdt (1994) for incorporating site effects into design spectra.

3. Directional effects. The directional amplification is stronger in the N-component. This suggests that tuned mass dampers could be installed inside the pier. They would accommodate asymmetric seismic demands. This recommendation is conceptual only, requiring multi-azimuth validation.

4. Design validation. The DAG telescope has already been designed with these principles in mind. The telescope design specification required all resonant frequencies to exceed 8 Hz (Özyazıcıoğlu & Yeşilyaprak, 2026). In situ impact hammer testing of the completed pier-foundation system confirmed this design choice. The fundamental frequency was measured at 76 Hz. This is well separated from the mountain's 0.85 Hz topographic resonance. The design successfully avoided the amplified frequency band identified in this study. Thus, site-specific topographic amplification should be considered early in the design process for critical infrastructure at mountain peaks.

5. Baseline for future expansion. This study provides a seismic baseline for the possible expansion of the DAG site. The undeveloped adjacent peaks G1, G3, and G4 are allocated for future optical and radio telescope projects (Figure 1). This work establishes the frequency-dependent topographic amplification and its spatial variability across the mountain profile. This provides an essential input for site selection of future instruments. The results also inform about resonance avoidance. This seismic characterisation ensures that the DAG site can accommodate new facilities with operational integrity under seismic loading.

5.4 Comparison of SSR and PSA Amplification

The SSR and PSA amplification estimates are considerably different. The SSR_{GM} reaches 3.89 at 0.85 Hz. The PSA ratio at the same frequency is only 1.8. This discrepancy reflects a fundamental distinction between these two measures. The SSR ratio is computed from Fourier amplitude spectra. Therefore, it reflects the raw frequency content of the ground motion. In contrast, PSA describes the response of a damped single degree of freedom (SDOF) system. The damping in the SDOF model smooths peaks, naturally yielding a lower amplification than the SSR counterpart.

The two metrics thus provide complementary insights. The Fourier SSR value of 3.89 at 0.85 Hz is a narrowband resonant peak. Its bootstrap median of 2.06 serves as a conservative lower bound due to spectral smearing. The resampling scheme with a truncated time window smears the peak. The full-window value of 3.89 is therefore an upper estimate of the narrow-band amplification. By contrast, the PSA ratio of 1.80 at T = 1.18 s is the design-oriented quantity. PSA amplification exceeds the code maximum of 1.4 by 28%. Its bootstrap 90% confidence interval [1.15, 2.73] lies above unity. This supports the statistical significance of the amplification.

This distinction has practical consequences for evaluating code provisions. The amplification factors in the building codes are proposed to scale the response spectrum (Borcherdt, 1994), not the SSR. Therefore, the PSA ratio of 1.80 is appropriate for comparison. The empirical amplification at the

resonance exceeds the maximum code factor by 28-62%. Because the analysis is based on a single event, this observation should be treated as preliminary.

5.5 Limitations and Future Work

The 16 September 2022 Mw 4.9 Çat earthquake is the single event this study relies on. This earthquake was the second largest event recorded by the EKONA and ETEKE stations since their installation. The largest was the 6 February 2023 Maraş earthquake of M_w = 7.8 (USGS, 2023), whose waveforms were unusable due to peak clipping. Although the bootstrap analysis offers quantitative uncertainty estimates, the results should be regarded as preliminary. This is because the site response is known to vary with earthquake magnitude, source mechanism, source−to−site distance, and azimuth angle (Bonilla et al., 2002; Steidl et al., 1996).

An additional limitation concerns the reference site. Like any rock site, ETEKE exhibits its own HVSR peaks, 3.52 at 0.55 Hz and 3.82 at 1.30 Hz (Figure 5; Table 2), which indicate that it is not entirely free of local site response. These peaks, however, fall outside the 0.85 Hz resonance band of the DAG crest and both stations are on competent bedrock classified as Soil Class A (Çomaklı, 2012; Kiper, 2013). At the frequency of interest of 0.85 Hz, ETEKE shows HVSR = 1.82, which is modest compared to EKONA's 10.11. The SSR at 0.85 Hz is therefore a reasonable approximation of the topographic amplification at the crest. To the extent that a residual reference-site bias exists, it would inflate the denominator (ETEKE amplitude) and thus make the true amplification of the crest larger than the 3.89 reported here. The reported value should therefore be treated as a conservative lower bound. The bootstrap analysis in Section 3.5 quantifies the resampling variability of the record and does not address this bias. As discussed in section 2.3, since EKONA is farther from the source than ETEKE, the path attenuation makes the SSR value of 3.89 a conservative lower bound on the true topographic amplification.

Recordings from future earthquakes will be essential to confirm the frequency−dependent amplification observed here. The planned installation of a third station at the summit in 2027 will help quantify the reference-site bias and provide a more complete characterisation of the topographic amplification across the mountain profile. This 3-instrument array will continue to provide valuable data. Particularly, this array will be useful in seismic response evaluation of adjacent G1, G3, and G4 peaks. The DAG site is expected to expand with additional optical and radio telescopes in the future. The data will help assess the seismic suitability of all the peaks.

6. Conclusions

This study evaluated topographic site effects at the DAG observatory using data from the Mw 4.9 Çat earthquake. The SSR and HVSR methods were applied to recordings from two seismic stations, namely ETEKE at the mountain base and EKONA near the summit. Both techniques identified a fundamental topographic resonance at 0.85 Hz. The absence of this resonant frequency at ETEKE confirms its topographic origin. The SSR geometric mean amplification at 0.85 Hz is 3.89. This value is substantially higher than near unity values typical of flat rock sites (Boore and Joyner, 1997). The HVSR analysis also identifies the same resonant frequency.

The PSA amplification ratio at T = 1.18 s is 1.80. This value exceeds the maximum amplification factor given by PS92 and Eurocode 8. This observation is based on a single event at a single azimuth. Multi-event validation is required before the code factors can be considered inadequate for the DAG site.

The implications for the DAG telescope design are also significant. The design specifications for the DAG telescope required all resonant frequencies to be higher than 8 Hz. In situ measurements confirmed a fundamental frequency of 76 Hz for the pier. This is well separated from the 0.85 Hz topographic resonance. The design therefore successfully avoided the site amplification identified in

this study. This finding underlines the value of considering topographic effects from the earliest stages of design.

Although this study is based on a single earthquake, confidence in the findings rests on converging lines of evidence and on quantitative uncertainty bounds. The SSR and HVSR methods identify the same resonant frequency of 0.85 Hz; while this agreement is not fully independent - both use the same horizontal components - it is corroborated by the absence of the peak at the base station, the consistency of the PSA response spectra, and the independent ambient-noise H/V measurement (Figure 6). The moving-block bootstrap yields a 90% confidence interval of [1.15, 2.73] for the PSA ratio at T = 1.18 s. Because the lower bound remains above unity, the observed broadband amplification represents a statistically robust feature of the site rather than a random fluctuation. However, the results remain preliminary and require validation with future recordings from events at complementary source azimuths. Such ground motion recordings will also allow directional effects to be assessed.

Acknowledgments

The authors thank the Turkish National Observatories (TUG) and the DAG telescope project team for the waveform data.

Statements and Declarations

Funding: The authors declare no funds, grants, or other support.

Disclosures: The authors declare no competing interests.

Author Contributions: Conceptualization, M.Ö.; Methodology, M.Ö.; Software, M.Ö.; Validation, M.Ö.; Formal Analysis, M.Ö.; Investigation, M.Ö., C.Y.; Resources, M.Ö., C.Y.; Data Curation, M.Ö., C.Y.; Writing – Original Draft, M.Ö.; Writing – Review and Editing, M.Ö., C.Y.; Visualization, M.Ö.; Supervision, M.Ö.; Project Administration, C.Y. All authors read and agreed to the published version.

Code and Data Availability: Raw waveform data are archived at the Turkish National Seismic Network (AFAD) under station codes ETEKE and EKONA. Requests should be directed to AFAD. The processed time histories, spectra, bootstrap replicates, and analysis scripts are available from the corresponding author on reasonable request.

AI Use: AI tools were used solely for grammar and punctuation refinement during the writing process. No AI tools were used for data analysis, interpretation, or generation of conclusions. All figures, tables, and numerical results were generated by the authors.

References

1. AFAD (2018) Türkiye Bina Deprem Yönetmeliği [Turkish Building Earthquake Code]. Afet ve Acil Durum Yönetimi Başkanlığı, Ankara. Resmî Gazete, 18 Mart 2018, Sayı: 30364 (Mükerrer). Available at: https://www.afad.gov.tr/tr/24210/Turkiye-Bina-Deprem-Yonetmeligi (Accessed: 7 September 2026).
2. Aki, K. & Richards, P.G. (2002). Quantitative Seismology (2nd ed.). University Science Books.
3. Assimaki, D., Gazetas, G., & Kausel, E. (2005). Effects of topographic and soil variability on the seismic response of slopes. Soil Dynamics and Earthquake Engineering, 25(7-10), 735-747.

4. Association Française de Normalisation (1995). Règles de construction parasismique – Règles PS applicables aux bâtiments. NF P06-013.
5. Bard, P.Y. (1999). Microtremor measurements: A tool for site effect estimation? In The Effects of Surface Geology on Seismic Motion, 1251-1279.
6. Bonilla, L.F., Steidl, J.H., & Lindley, G.T. (2002). Site amplification in the San Fernando Valley, California: Variability of site-effect estimation using the S-wave, coda and HVSR methods. Bulletin of the Seismological Society of America, 92(2), 710-730.
7. Boore, D.M. & Joyner, W.B. (1997). Site amplifications for generic rock sites. Bulletin of the Seismological Society of America, 87(2), 327-341.
8. Boore, D.M. (1972). A note on the effect of simple topography on seismic SH waves. Bulletin of the Seismological Society of America, 62(1), 275-284.
9. Borcherdt, R.D. (1970). Effects of local geology on ground motion near San Francisco Bay. Bulletin of the Seismological Society of America, 60(1), 29-61.
10. Borcherdt, R.D. & Gibbs, J.F. (1976). Effects of local geological conditions in the San Francisco Bay region on ground motions and the intensities of the 1906 earthquake. Bulletin of the Seismological Society of America, 66(2), 467-500.
11. Borcherdt, R.D. (1994). Estimates of site-dependent response spectra for design (methodology and justification). Earthquake Spectra, 10(4), 617-653.
12. Bouchon, M. & Barker, J.S. (1996). Seismic response of a hill: The example of Tarzana, California. Bulletin of the Seismological Society of America, 86(1), 66-72.
13. Bouchon, M., Schultz, C.A., & Toksöz, M.N. (1996). Effect of three-dimensional topography on seismic motion. Journal of Geophysical Research, 101(B3), 5835-5846.
14. Chávez-García, F.J. & Cárdenas-Soto, M. (2002). The contribution of the horizontal-to-vertical spectral ratio of microtremors to site effect evaluation. Journal of Earthquake Engineering, 6(1), 1-20.
15. Chávez-García, F.J. & Faccioli, E. (2000). Complex site effects and building codes: Making the leap. Journal of Seismology, 4(1), 23-40.
16. Çomaklı, K. (2012) Geophysical site investigation of DAG (in Turkish). K. Çomaklı Geotechnical Engineering Ltd, Co, Erzurum.
17. Del Gaudio, V., Coccia, S., Wasowski, J., Gallipoli, M.R., & Mucciarelli, M. (2008). Detection of directivity in seismic site response from microtremor spectral analysis. Natural Hazards and Earth System Sciences, 8(4), 751-762. doi:10.5194/nhess-8-751-2008.
18. Dobry, R., Borcherdt, R.D., & Crouse, C.B. (2000). New site coefficients and site classification system used in recent building seismic code provisions. Earthquake Spectra, 16(1), 41-67.
19. Efron, B. & Tibshirani, R.J. (1993). An Introduction to the Bootstrap. Chapman & Hall, New York.
20. Emre, Ö., Duman, T.Y., Özalp, S., Şaroğlu, F., Olgun, Ş., Elmacı, H., & Çan, T. (2013). Active fault map of Turkey with an explanatory text, 1:1,250,000 scale. General Directorate of Mineral Research and Exploration (MTA), Special Publication Series, 30, Ankara.
21. European Committee for Standardization (2004a). Eurocode 8: Design of structures for earthquake resistance – Part 1: General rules, seismic actions and rules for buildings. EN 1998-1:2004.
22. European Committee for Standardization (2004b). Eurocode 8: Design of structures for earthquake resistance – Part 5: Foundations, retaining structures and geotechnical aspects. EN 1998-5:2004.
23. Faccioli, E. (1991). Seismic amplification in the presence of geological and topographic irregularities. Proceedings of the 2nd International Conference on Recent Advances in Geotechnical Earthquake Engineering and Soil Dynamics, 1779-1797.
24. Fäh, D., Kind, F., & Giardini, D. (2001). A theoretical investigation of the HVSR technique for site response estimation. Bulletin of the Seismological Society of America, 91(4), 752-767.

25. Fäh, D., Rüttener, E., & Hugenschmidt, J. (1997). A microtremor study for the site response estimation in the city of Basel, Switzerland. Soil Dynamics and Earthquake Engineering, 16(7-8), 441-454.
26. Field, E.H. & Jacob, K.H. (1995). A comparison and test of various site-response estimation techniques, including three that are not reference-site dependent. Bulletin of the Seismological Society of America, 85(4), 1127-1143.
27. Ganbat, B., Yoshizawa, K., Meltzer, A., & Stachnik, J. (2026). Spatial distribution of coda Q in Hangay Dome, Mongolia. Tectonophysics, 231293. https://doi.org/10.1016/j.tecto.2026.231293
28. Geli, L., Bard, P.Y., & Jullien, B. (1988). The effect of topography on earthquake ground motion: A review and new results. Bulletin of the Seismological Society of America, 78(1), 42-63.
29. Güralp 6-TD. Support Documentation. https://www.guralp.com/howtos/complete-6td-installation/: (Accessed: 05.09.2026, 16:00)
30. Hartzell, S., Carver, D., & King, K.W. (1994). Initial investigation of site and topographic effects at Robinwood Ridge, California. Bulletin of the Seismological Society of America, 84(5), 1336-1349.
31. Havskov, J; Sørensen, M.B.; Vales, D.; Özyazıcıoğlu, M.; Sánchez, G.; Li. B. (2016). Coda Q in Different Tectonic Areas, Influence of Processing Parameters. Bulletin of the Seismological Society of America, 106 (3), 956–970. https://doi.org/10.1785/0120150359
32. Jarvis, A., Reuter, H.I., Nelson, A., & Guevara, E. (2008). Hole-filled SRTM for the globe Version 4. Available from the CGIAR-CSI SRTM 90m Database. https://srtm.csi.cgiar.org
33. Kiper B (2013). Geotechnical and geophysical site investigation of DAG (in Turkish). Bulent Kiper Geotechnical Engineering Ltd, Co, Gaziosmanpaşa, Ankara.
34. Kramer, S.L. (1996). Geotechnical Earthquake Engineering. Prentice Hall.
35. Künsch, H.R. (1989). The jackknife and the bootstrap for general stationary observations. The Annals of Statistics, 17(3), 1217–1241. https://doi.org/10.1214/aos/1176347265
36. Lermo, J. & Chávez-García, F.J. (1993). Site effect evaluation using spectral ratios with only one station. Bulletin of the Seismological Society of America, 83(5), 1574-1594.
37. Maufroy, E., Cruz-Atienza, V.M., & Cotton, F. (2015). Frequency-dependent site amplification in the Mexico City basin from weak motion records. Bulletin of the Seismological Society of America, 105(2A), 677-693.
38. Mucciarelli, M. & Gallipoli, M.R. (2001). A critical review of 10 years of microtremor HVSR technique. Bollettino di Geofisica Teorica ed Applicata, 42(3-4), 255-266.
39. Nakamura, Y. (1989). A method for dynamic characteristics estimation of subsurface using microtremor on the ground surface. Quarterly Report of the Railway Technical Research Institute, 30(1), 25-33.
40. Ottemöller L, Voss P & Havskov J (2013) Seisan earthquake analysis software for Windows, Solaris, Linux And MacOsx, Software Manual V.9.0
41. Ozyazıcıoğlu, M., & Yeşilyaprak, C. (2026). In situ measurement of resonant frequencies of a large cylindrical pier of a major telescope. Journal of Civil Structural Health Monitoring, 16, Article 18. https://doi.org/10.1007/s13349-025-01046-1
42. Ozyazıcıoğlu, M., Kartal, R.F., Kılıç, T., & Yeşilyaprak, C. (2024). Probabilistic seismic hazard evaluation of eastern Anatolia observatory. Arabian Journal of Geosciences, 17(1). doi:10.1007/s12517-023-11834-y
43. Ozyazicioglu, M., Ottemöller, L., Kılıç, T. et al. (2020) Ambient noise levels in Turkey and an evaluation of recording quality of the National Network. Acta Geodaetica et Geophysica 55, 83–99 https://doi.org/10.1007/s40328-019-00282-4
44. Pagliaroli, A., Pitilakis, K., Chávez-García, F.J., & Raptakis, D. (2014). Experimental study of topographic effects using explosions and microtremor recordings. Bulletin of Earthquake Engineering, 12(4), 1405-1428. doi:10.1007/s10518-013-9551-3.
45. Paolucci, R. (2002). Amplification of earthquake ground motion by steep topographic irregularities. Earthquake Engineering & Structural Dynamics, 31(10), 1831-1853.

46. Pitilakis, K.D. (ed) (2007) Earthquake Geotechnical Engineering: 4th International Conference on Earthquake Geotechnical Engineering - Invited Lectures. Springer, Dordrecht. https://doi.org/10.1007/978-1-4020-5893-6
47. Pitilakis, K., Raptakis, D., & Makra, K. (2013). Overview of topographic effects based on experimental observations: Meaning, causes and possible interpretations. Geophysical Journal International, 194(3), 1537-1550.
48. Rovelli, A., Caserta, A., & Marra, F. (1991). Topographic effects on the seismic response of the Colle di Roio area (central Italy). Earthquake Engineering & Structural Dynamics, 20(12), 1145-1159.
49. Sanchez-Sesma, F.J. & Campillo, M. (1991). Diffraction of P, SV, and Rayleigh waves by topographic features: A boundary integral formulation. Bulletin of the Seismological Society of America, 81(6), 2234-2253.
50. Shearer, P.M. (2009). Introduction to Seismology (2nd ed.). Cambridge University Press.
51. Spudich, P., Hellweg, M., & Lee, W.H.K. (1996). Directional topographic site response at Tarzana observed in aftershocks of the 1994 Northridge, California earthquake. Bulletin of the Seismological Society of America, 86(1B), S193-S208.
52. Steidl, J.H., Tumarkin, A.G., & Archuleta, R.J. (1996). What is a reference site? Bulletin of the Seismological Society of America, 86(6), 1733-1748.
53. Styron, R. & Pagani, M. (2020). The GEM Global Active Faults Database. Earthquake Spectra, 36(1_suppl), 160-180. https://doi.org/10.1177/8755293020944182
54. Sun, Y. & Li, Y. (2012). A state-of-the-practice review on amplification of earthquake ground motion resulting from surface topographic effects. Proceedings of the 15th World Conference on Earthquake Engineering.
55. USGS (2023). M 7.8 - 26 km ENE of Nurdağı, Turkey. United States Geological Survey Earthquake Hazards Program. Available at: https://earthquake.usgs.gov/earthquakes/eventpage/us6000jllz
56. Yalcinkaya, E. & Alptekin, O. (2005). Site Effect and its Relationship to the Intensity and Damage Observed in the June 27, 1998 Adana-Ceyhan Earthquake. Pure and Applied Geophysics, 162, 913–930. https://doi.org/10.1007/s00024-004-2648-5
57. Zaslavsky, Y., Shapira, A., & Gorstein, M. (2000). Amplification effects from earthquakes and ambient noise in the Dead Sea rift (Israel). Soil Dynamics and Earthquake Engineering, 20(1-4), 187-207. doi:10.1016/S0267-7261(00)00044-7.
58. Zhou, H. (2018). Review on the study of topographic effect on seismic ground motion. Earthquake Science, 31(2), 110-118.

Supplementary Files

This is a list of supplementary files associated with this preprint. Click to download.

- AppendixA.docx